energy&fuels

Article

pubs.acs.org/EF

Modifications of Carbonate Fracture Hydrodynamic Properties by CO_2-Acidified Brine Flow

Hang Deng,[†] Brian R. Ellis,[†,‡] Catherine A. Peters,[*,†] Jeffrey P. Fitts,[†] Dustin Crandall,[§,∥] and Grant S. Bromhal[§]

[†]Civil and Environmental Engineering, Princeton University, Princeton, New Jersey 08544, United States

[§]National Energy Technology Laboratory, 3610 Collins Ferry Road, Morgantown, West Virginia 26507, United States

[∥]URS Corporation, 3610 Collins Ferry Road, Morgantown, West Virginia 26507, United States

ABSTRACT: Acidic reactive flow in fractures is relevant in subsurface activities, such as CO_2 geological storage and hydraulic fracturing. Understanding reaction-induced changes in fracture hydrodynamic properties is essential for predicting subsurface flows, such as leakage, injectability, and fluid production. In this study, X-ray computed tomography scans of a fractured carbonate caprock were used to create three-dimensional (3D) reconstructions of the fracture before and after reaction with CO_2-acidified brine (Ellis, B.; Peters, C.; Fitts, J.; Bromhal, G.; McIntyre, D.; Warzinski, R.; Rosenbaum, E. Deterioration of a fractured carbonate caprock exposed to CO_2-acidified brine flow. *Greenhouse Gases: Sci. Technol.* **2011**, *1*, 248−260). As expected, mechanical apertures were found to increase substantially, doubling and even tripling in some places. However, the surface geometry evolved in complex ways, including "comb-tooth" structures created from preferential dissolution of calcite in transverse sedimentary bands and the creation of degraded zones, i.e., porous calcite-depleted areas on reacted fracture surfaces. These geometric alterations resulted in increased fracture roughness, as measured by surface Z_2 parameters and fractal dimensions D_f. Computational fluid dynamics (CFD) simulations were conducted to quantify the changes in hydraulic aperture, fracture transmissivity, and permeability. The results show that the effective hydraulic apertures are smaller than the mechanical apertures and the changes in hydraulic apertures are nonlinear. Overestimation of the flow rate by a factor of 2 or more would be introduced if fracture hydrodynamic properties were based on mechanical apertures or if hydraulic aperture is assumed to change proportionally with mechanical aperture. The differences can be attributed, in part, to the increase in roughness after reaction and is likely affected by contiguous transverse sedimentary features. Hydraulic apertures estimated by the one-dimensional (1D) statistical model and two-dimensional (2D) local cubic law (LCL) model are consistently larger than those calculated from the CFD simulations. In addition, a novel ternary segmentation method was devised to handle the degraded zones, allowing for a bounding analysis of the effects on hydraulic properties. We found that the degraded zones account for less than 15% of the fracture volume but cover 70−80% of the fracture surface. When the degraded zones are treated as part of the fracture, the fracture transmissivities are 2−4 times larger because the fracture surfaces after reaction are not as rough as they would be if one considers the degraded zone as part of the rock. Therefore, while degraded zones created during geochemical reactions may not significantly increase mechanical aperture, this type of feature cannot be ignored and should be treated with prudence when predicting fracture hydrodynamic properties.

INTRODUCTION

Understanding changes of fracture hydrodynamic properties as a result of contact with acidic fluids is essential in numerous subsurface activities, such as geological storage of CO_2, shale gas production, geothermal energy extraction, and nuclear waste disposal. Fractures are of special importance because of their prevalence[1] and potential impacts on flow and reactive transport.[2] Both natural and induced fractures are widely documented in subsurface systems,[3−5] including CO_2 storage sites.[6,7] Geomechanical studies have demonstrated that, during CO_2 injection, fractures can be created, activated, and propagate in caprocks because of shear stresses,[8] thermal stresses,[9] and crystallization.[10] Because fractures serve as conduits for flow, their presence may enhance the risks of CO_2 leakage. Therefore, a comprehensive assessment of caprock integrity requires detailed characterization of fracture hydrodynamic properties and knowledge of their evolution over time. During shale gas and geothermal energy extraction, fractures are often intentionally induced. Their hydrodynamic properties control the production and, hence, profitability of the fields.

Fractures provide pathways for transport of reactive solutes, resulting in thermodynamic gradients that accelerate water−rock interactions. Geochemical alterations of fracture surfaces and flow-path geometry will ultimately modify hydrodynamic properties of caprocks or production formations. In the context of CO_2 geological storage, both simulation results[11] and experiments[12−14] have shown profound alteration of fracture geometry because of the flow of CO_2-acidified brines. Similarly, acidic fracturing fluids may be used to alter the hydrodynamic properties of fractures created or activated during the

Special Issue: Accelerating Fossil Energy Technology Development through Integrated Computation and Experiment

Received: December 10, 2012
Revised: April 4, 2013
Published: April 8, 2013

exploitation of gas-bearing shale formations. Although shale formations typically have a high content of relatively unreactive clay minerals, they often coexist with other acid-soluble minerals, e.g., carbonates.[15] Furthermore, if induced fractures are not properly contained within the production formation but instead propagate into the overlying formations, the hydrodynamic properties of these fractures and their evolution will determine the risks of vertical migration of fracturing fluid and gas and potentially groundwater pollution.

Reactive transport in fractures and the patterns of dissolution and precipitation are controlled by the flow regime,[16−18] initial geometry,[2,18] confining stress,[17] mineralogy and brine chemistry.[13,14] Numerous simulation studies have investigated the evolution of fracture aperture and hydrodynamic properties that result from the interactions between fracture surfaces and reactive flow.[18−23] In addition, imaging techniques, such as light transmission[24] and three-dimensional (3D) micro X-ray computed tomography (xCT),[25−28] provide non-invasive geometric measurement tools, and their applications have enabled observations of acid-driven geometric evolution of fractures.[16,17,25,29,30] Detwiler[17] observed relatively uniform dissolution at a low Damkohler number and channelization at a high Damkohler number. This same research group also reported that a low Peclet number favors the formation of channels, while a high Peclet number leads to smoothing of small scale roughness without channelization.[16] Furthermore, Szymczak and Ladd[23] found that channelization occurs above a roughness threshold and is favored under the conditions of high reaction rates and an intermediate Peclet number. While these studies have greatly advanced our knowledge of some fundamental processes underlying geochemically driven fracture evolution, they often assumed homogeneous mineralogy and used model fractures.

The effects of mineral spatial heterogeneity on fracture evolution are poorly understood and need consideration because mineral heterogeneity may result in very complex geometric modifications. In a high-pressure experiment, Ellis et al.[13] flowed CO_2-acidified brine through an artificially fractured carbonate core from the Amherstburg formation of the Michigan sedimentary basin. Post-experiment scanning electron microscopy (SEM) imaging revealed extensive dissolution and complex geometric alterations of the fracture created by preferential dissolution patterns, as shown in Figure 1. For example, where the relatively soluble mineral calcite is banded with less soluble dolomite, preferential dissolution of calcite created "comb-tooth"-shaped roughness (Figure 1a). In contrast, where calcite is homogeneously mixed with dolomite or non-reactive clay minerals and quartz, very porous calcite-depleted areas were formed, which the authors refer to as "degraded zones" (Figure 1b).

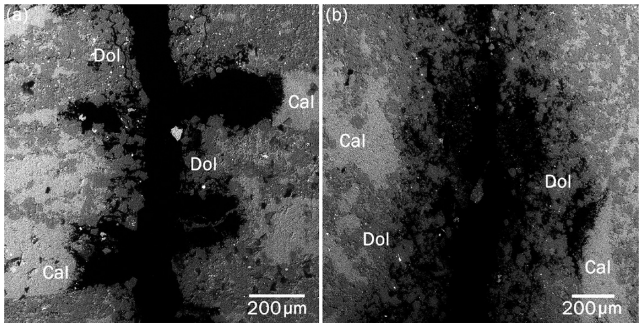

Figure 1. SEM images in backscattered electron (BSE) mode, showing unique fracture surface geometries that resulted from the reaction with CO_2-acidified brine (as a result of the experiment presented in ref 13): (a) comb-tooth wall geometry resulting from receding calcite bands and persistence of less soluble minerals and (b) porous "degraded zone" along the fracture wall created by preferential dissolution of calcite.

It remains an open question as to whether extensive fracture volume increases resulting from dissolution will manifest as substantial alterations to fracture hydrodynamic properties and thereby compromise caprock sealing capacity. It is possible that geometric alterations, such as increased roughness, will counteract the impact of fracture volume increase. In an experiment flowing acidic water through a fractured argillaceous limestone rock sample, Noiriel et al.[30] recorded a decrease in permeability that they attributed partly to the increase of fracture roughness.

A large volume of literature exists on fracture roughness and its impacts on flow. One-dimensional (1D) models based on the distribution of local apertures have been proposed to incorporate roughness using a weighted average or standard deviation of apertures.[31−33] Another modeling approach widely adopted is the local cubic law (LCL).[18,19,34−37] It assumes that the cubic law for smooth parallel wall fractures holds locally and solves the Reynolds equation locally. However, these models do not provide accurate estimations of fracture hydrodynamic properties at relatively high yet realistic roughness.[29,38,39]

Computational fluid dynamics (CFD) simulations have been shown to provide accurate calculations for flow in fractures across a range of plausible fracture roughness.[38−40] Using different meshing tools and applying different degrees of smoothing, Crandall et al.[39] generated six fracture meshes with different degrees of roughness. They found that an increase in fracture roughness results in more tortuous flow and lower transmissivity. However, roughness in these studies has typically been decoupled from the spatial distributions of minerals and the resulting dissolution patterns.

In this study, our objective was to investigate the relationships between the change in fracture surface geometry and hydrodynamic properties resulting from acid-promoted dissolution. In particular, we investigated the effects of significant fracture volume increase and roughness increase that arise because of mineral spatial heterogeneities. On the basis of the outcome of the experiment by Ellis et al.,[13] xCT scans of the fractured core were used to reconstruct the fracture geometries before and after reaction with flowing CO_2-acidified brines. CFD simulations were performed on 3D finite-element meshes generated from the fracture geometries, allowing for a comparison of the predicted hydrodynamic aperture to the mechanical aperture. To determine if simpler modeling approaches can capture fracture surface geometry effects, hydrodynamic properties were also estimated using a 1D statistical model and a two-dimensional (2D) LCL model. The basis for comparison of these model predictions are the fracture hydrodynamic properties calculated from the CFD simulation results. It was not possible to make comparisons to experimental permeabilities, which were not measurable under the flow condition of the experiment, as explained by Ellis et al.[13]

Our study is novel in two aspects. First, the fracture geometries used are the actual results from the reaction of a caprock specimen, which is a typical dolomitic limestone that is rich in mineral heterogeneity. Second, we developed a novel segmentation approach to examine the effect of degraded zones, i.e., the calcite-depleted porous rock on reacted fracture surfaces.

THEORETICAL BASIS

Fracture transmissivity, T, and permeability, k, are both measurements of the ease for fluid to flow through a fracture, as described by the relationship between the volumetric flow rate, Q, and the pressure gradient ∇P through Darcy's law

$$Q = -T\frac{(\nabla P)}{\mu} = -\frac{Ak}{\mu}\nabla P \quad (1)$$

where μ is the fluid viscosity and A is the cross-sectional area of the fracture perpendicular to flow. The theory for single-phase flow in a smooth parallel fracture,[41] frequently referred to as the cubic law, states that T is related to the cube of mechanical aperture, b, the vertical distance between two fracture walls. When the assumption of smooth parallel walls breaks down, the aperture is replaced with its effective value, the hydraulic aperture b_h[33]

$$T = -\frac{Wb_h^3}{12} \quad (2)$$

$$k = \frac{b_h^2}{12} \quad (3)$$

where w is the width of the fracture. Properties T, k, and b_h provide three different ways to characterize fracture hydrodynamic properties, and they are related as shown in eqs 1−3. The value of the fracture T and fracture intrinsic k is that they can be directly compared to field measurements, lending insight on how the fracture may impact the hydrodynamic properties of the formation. The b_h can be readily compared to b, which can be derived from image analyses or estimated from fracture volume, to investigate whether and how the flow behaves differently from the flow in a parallel wall fracture.

METHODS

Segmentation and Meshing. The xCT scans used in this study had voxel resolution of 27 μm. Two separate areas of the fracture were selected to avoid regions that were not amenable to meshing, including a horizontal fracture and the multifractured edges. The selected fracture areas have a length of 2.176 and 3.078 cm for Area-1 and Area-2, respectively, and a width of 1.296 cm for both areas (Figure 2). xCT images corresponding to the selected fracture areas were processed to isolate the fractures and rock matrix immediately surrounding the fracture boundary on the grayscale xCT images. To segment the grayscale xCT images, we applied Otsu's method,[42] which involves searching for thresholds that minimize interclass variance. As an example, panels a and c of Figure 3 show the grayscale xCT image for a cross-sectional slice before the reaction. Figure 3b is the histogram for the boxed area of Figure 3a, showing the threshold generated by Otsu's method. The resulting binary segmentation separating the fracture from the rock is shown in Figure 3d.

The after reaction xCT images did not show a clean interface but instead showed fuzzy zones between the rock and the fracture (Figure 3g). These areas have been previously identified using SEM images of core sections (Figure 1b) as "degraded zones",[13] porous areas created by preferential dissolution of calcite from regions where it is intermixed with less reactive minerals. To examine the effect of depleted zones, a ternary segmentation method was devised to classify voxels as either a fracture, rock, or degraded zone (Figure 3h). This method did not simply segment voxels based on grayscale intensity, which would have overestimated the degraded zone because of the ubiquitous presence of transitional grayscale intensities at all edges. Instead, an algorithm was developed in which a window with a specific size moves along the rock−fracture interface to identify zones with intermediate grayscale intensities, and only zones with thickness above a cutoff value were segmented as the "degraded zone". A wide range of window sizes and cutoff thicknesses were tested. Numerous visual inspections were conducted to compare the ternary-segmented images to the original xCT images to ensure that the algorithm was accurately characterizing the degraded zone.

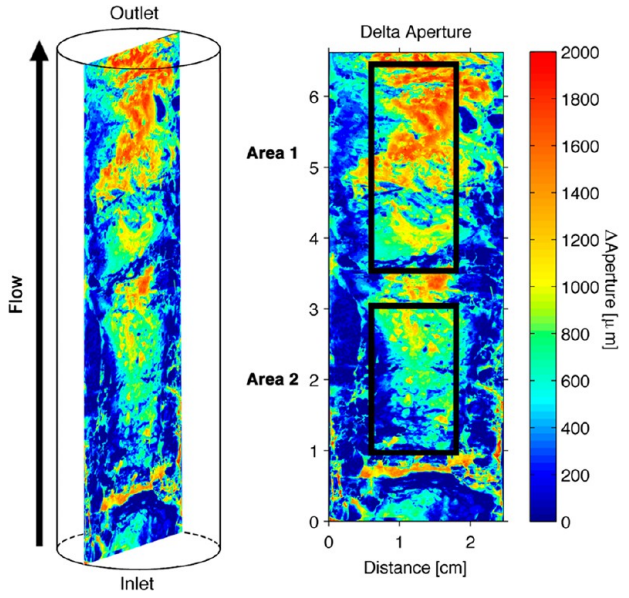

Figure 2. Schematic of the fractured core (left) with a map of fracture aperture change because of reactions with CO_2-acidified brine flow (on the basis of ref 13), with black boxes indicating two areas selected for CFD simulation in this study (right) (this map is different from the aperture change maps generated in this work, because a binary segmentation was performed for both before and after reaction xCT images).

To examine the impact of the degraded zones on flow, a bounding analysis was conducted to constrain reality between two extremes. In one scenario, the degraded zones were treated as part of the rock (Figure 3i), assuming that the degraded zones are impermeable. In the other scenario, the degraded zones were treated as part of the fracture (Figure 3j), assuming no resistance to flow. Reality falls somewhere between these two scenarios. Comparing flow in the two scenarios provides some insight on the impacts of the degraded zone on fracture hydrodynamic properties.

The segmented images were imported into a 3D volumetric mesh generator iso2mesh,[43] producing meshes such as that shown in Figure 4. Given the complexity of the fracture geometry, unstructured tetrahedral meshes were generated. Minimal smoothing and simplifications were applied to preserve the complexity of the fracture geometries. Meshing parameters were optimized to ensure good mesh quality (e.g., orthogonality and skewness) and numerical performance (e.g., convergence and computational cost). Six 3D meshes were generated, including three meshes each for Area-1 and Area-2: before reaction binary segmentation, after reaction with the degraded zone treated as a rock, and after reaction with the degraded zone treated as a fracture. Each mesh contains on the order of 10^6 grids following optimization.

To quantify uncertainties deriving from the choice of mesh density, a smaller area of Area-2 was analyzed using a range of mesh densities. Specifically, the selected Area-2 fracture was the after reaction mesh with degraded zones treated as a rock. This test area was regarded to be the best case for the study of sensitivity to mesh density for two reasons. First, its geometry is the most difficult to mesh, which requires finer grids to capture sharp features. Second, the apertures of the test area cover a wide range of the aperture values of the whole area, ranging from 0 to 1998 μm. Meshes of the test area were generated using a spectrum of meshing parameters, resulting in density increases by a factor of 2−20. CFD simulations of these test meshes showed that higher mesh densities result in slightly lower values of hydraulic aperture. An increase of the mesh density by more than 20 times leads to a decrease of 28 μm.

dx.doi.org/10.1021/ef302041s | Energy Fuels 2013, 27, 4221−4231

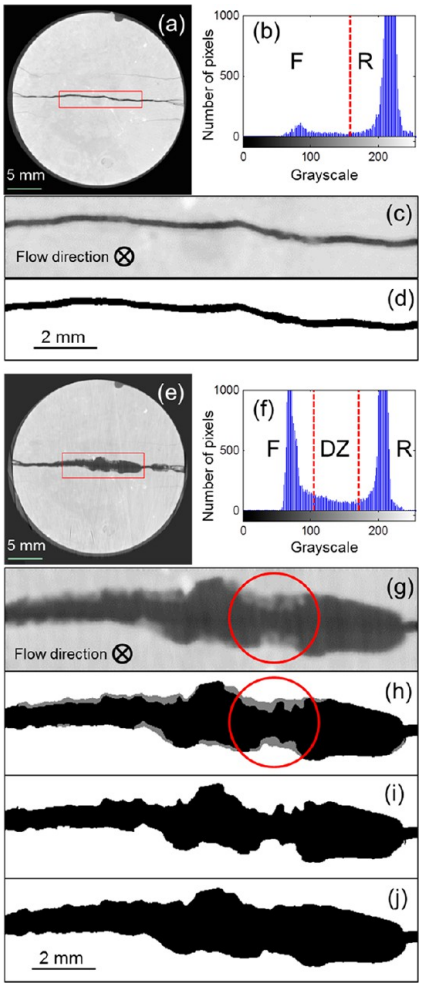

Figure 3. Example images depicting the geometry of the fracture, with a focus on the degraded zone and the ternary segmentation method developed in this work. The location for these images is in Area-2 at y = 5.75 cm according to the scale shown in Figure 2: (a) xCT image of a cross-section of the fracture taken before the experiment, with the study area identified in the red box, (b) histogram for the grayscale image of the study area in panel a, with F corresponding to the fracture and R corresponding to the rock, (c) close-up of the grayscale xCT image of the study area in panel a, (d) segmented image, with black corresponding to the fracture and white corresponding to the rock, (e) xCT image of the same fracture cross-section, taken after the experiment, with the study area indicated in the red box, (f) histogram for the grayscale image of the study area in panel e, with F corresponding to the fracture, R corresponding to the rock, and DZ corresponding to degraded zones, (g) close-up of the grayscale xCT image, with a circle indicating an area where there is a degraded zone, (h) ternary segmented image with degraded zones shown in gray, (i) binary segmented image showing the degraded zone treated as a rock, and (j) binary segmented image showing the degraded zone treated as a fracture.

Therefore, we can assume that the uncertainty associated with mesh densities is approximately 28 μm.

Geometric Characterizations. To statistically characterize fracture surface geometries, each mesh was converted into a 3D volumetric image with the same voxel resolution of 27 μm as the original xCT images. The fracture aperture was measured as the total number of fracture pixels in each column spanning the two fracture walls in the 3D volumetric image.

Surface roughness was characterized using the surface Z_2 parameter and fractal dimension D_f. For a 3D surface with a resolution of Δx and

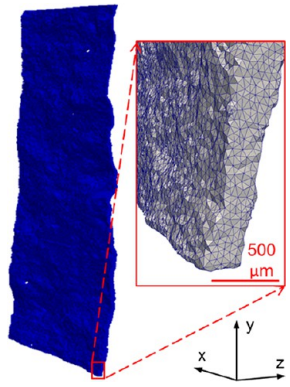

Figure 4. Finite-element tetrahedral mesh of Area-2 before reaction and a close-up of the mesh in the red box.

Δy on the x and y directions, respectively, the surface Z_2 parameter is calculated using eq 4[44]

$$Z_2 = \left\{ \frac{1}{(N_x - 1)(N_y - 1)} \left[\frac{1}{\Delta x^2} \sum_{i=1}^{N_x-1} \sum_{j=1}^{N_y-1} \frac{(z_{i+1,j+1} - z_{i,j+1})^2 + (z_{i+1,j} - z_{i,j})^2}{2} + \frac{1}{\Delta y^2} \sum_{j=1}^{N_y-1} \sum_{i=1}^{N_x-1} \frac{(z_{i+1,j+1} - z_{i+1,j})^2 + (z_{i,j+1} - z_{i,j})^2}{2} \right] \right\}^{1/2} \quad (4)$$

where N_x and N_y are the numbers of discrete grids along the x and y axes and z is the height of the surface. A large surface Z_2 parameter corresponds to large variation of the local surface slope and, thus, corresponds to higher roughness.

Fractal dimensions, D_f, for 2D cross-sections along the flow direction (y) were calculated using the bandwidth method.[39,45] Standard deviation of the vertical displacement, σ_S, was calculated using eq 5 for a range of window size, s.

$$\sigma_S = \sqrt{\frac{1}{N_y - s} \sum_{i=1}^{N_y - s} (z_{i+s} - z_i)^2} \quad (5)$$

The parameter s ranges from Δy and is cut off at the long wavelength, which is approximately $^1/_{16}$ of the length of the fracture.[46] A linear fitting was applied on the logarithms of σ_S and s to obtain the Hurst exponent, H. The fractal dimension, D_f, is then calculated from H using eq 7.

$$\sigma_S \propto s^H \qquad (0 < s < L/16) \quad (6)$$

$$D_f = 2 - H \quad (7)$$

For each fracture surface, calculations of the surface Z_2 parameter and D_f used a resolution (Δx and Δy) of 27 μm. The number of grids along the flow direction (y) is 806 and 1140 for Area-1 and Area-2, respectively, and the number of grids across the flow direction (x) is 480 for both areas. Therefore, there are 480 cross-sections along the flow direction for each surface. D_f was calculated for each cross-section, and the average is used for the surface. For each fracture geometry, surface Z_2 parameters and D_f were calculated for both the upper and lower fracture surfaces (which were assigned arbitrarily, because neither surface is up or down). Because the flow is affected by not only the surface roughness but also the degrees of matching between the upper and lower surfaces,[47] a midsurface[48] defined as the mean of the two fracture surfaces was used, providing a representation of the fracture undulation. Roughness of the midsurface was also characterized for all of the fracture geometries.

CFD Simulations. CFD simulations were conducted by importing the finite-element tetrahedral meshes into OpenFOAM (OpenCFD,

dx.doi.org/10.1021/ef302041s | Energy Fuels 2013, 27, 4221−4231

Table 1. Mesh Properties of Six Fracture Geometries[a]

			volume (mm^3)	number of grids	surface Z_2 parameter			D_f		
					upper wall	lower wall	midsurface	upper wall	lower wall	midsurface
Area-1	before reaction		1.68×10^2	3.76×10^6	0.85	0.97	0.67	1.33	1.36	1.29
	after reaction	DZF	3.38×10^2	6.41×10^6	0.97	0.98	0.69	1.39	1.41	1.33
		DZR	2.98×10^2	7.09×10^6	1.66	1.92	1.26	1.51	1.56	1.49
Area-2	before reaction		1.33×10^2	3.48×10^6	0.66	0.79	0.55	1.31	1.33	1.28
	after reaction	DZF	5.28×10^2	5.23×10^6	1.31	1.28	0.90	1.49	1.49	1.46
		DZR	4.21×10^2	9.79×10^6	2.17	2.27	1.52	1.57	1.57	1.56

[a]DZF, degraded zones treated as a fracture; DZR, degraded zones treated as a rock.

Ltd., ESI Group) and using its tools to numerically solve the continuity and momentum equations. A steady-state solver (simpleFoam) was used. Momentum was solved using the smoothSolver, and pressure was solved with the geometric−algebraic multigrid (GAMG) solver. The momentum and continuity equations were coupled using the semi-implicit method for pressure-linked equations (SIMPLE) algorithm. A linear scheme was used to interpolate values from the cell center to the face center, and a limited non-orthogonal correction with $\psi = 0.7$ was selected to evaluate the surface normal gradient from the gradient of values at the cell centers. The convergence criterion for steady state was set when the normalized residual in the solution falls below 10^{-5}.

Boundary conditions used in the simulations are no-slip wall, fixed pressure at the outlet, and uniform velocity profile at the inlet. The test velocities vary from 10^{-6} to 10^{-3} m/s, ensuring a flow regime of creeping flow, i.e., $Re < 1$. The Reynolds number (Re) was calculated for all fracture geometries, using the equation[49]

$$Re = \frac{4\rho Q}{p\mu} \tag{8}$$

where ρ is the fluid density and p is the perimeter of the channel. Perimeters were calculated for all of the fracture cross-sections perpendicular to flow direction in every fracture. The Reynolds number calculated from the velocity range and perimeter range vary between 2×10^{-4} and 0.44. Fluid properties of water were used in all of the simulations, with $\rho = 998.2$ kg/m^3 and $\mu = 10^{-3}$ Pa s. Four different velocities were used for each fracture geometry to capture variability in the calculations, which resulted in negligible variations in the simulation results, and therefore, only averages are reported for each mesh geometry. The CFD simulations resulted in pressure gradient fields, which together with the flow rate were used to calculate fracture T, k, and b_h using eqs 1−3.

One-Dimensional Empirical Model. For comparison, the 1D empirical model proposed by Zimmerman and Bodvarsson[33] was also used. The model (eq 9) estimates b_h from b and accounts for the impacts of roughness by incorporating the standard deviation of mechanical aperture, σ, and contact area ratio, c, the ratio of contact area over the fracture surface area.

$$b_h^{\,3} \approx \overline{b}^3\left[1 - \frac{1.5\sigma^2}{\overline{b}^2}\right](1 - 2c) \tag{9}$$

In this study, contact area ratios within Area-1 and Area-2 are negligible.

Two-Dimensional LCL Model. Also, for comparison, the 2D LCL model[35] was used. In this model, the cubic law is assumed applicable locally. The 2D steady-state mass balance equation is given in eq 10.

$$\frac{\partial}{\partial x}\left[b^3(x,y)\frac{\partial P(x,y)}{\partial x}\right] + \frac{\partial}{\partial y}\left[b^3(x,y)\frac{\partial P(x,y)}{\partial y}\right] = 0 \tag{10}$$

Five-point central finite difference numerical approximation was used to solve the equation at each cell, with the harmonic mean of the apertures of the adjacent cells taken as equivalent aperture on the edge. Vertically averaged velocities are then calculated from the pressure fields and Darcy's law (eqs 11 and 12).

$$\overline{u}_x = \frac{b(x,y)^2}{12\mu}\frac{\Delta P}{\Delta x} \tag{11}$$

$$\overline{u}_y = \frac{b(x,y)^2}{12\mu}\frac{\Delta P}{\Delta y} \tag{12}$$

RESULTS AND DISCUSSION

Fracture Geometric Characterization. Table 1 presents the mesh properties of six fracture geometries. The significant fracture volume increase caused by calcite dissolution is reflected in the higher numbers of cells for the four after reaction meshes (Table 1). The after reaction meshes also required finer grids at the geometrically sharp locations to accurately represent surface roughness. As demonstrated in panels a−c and e−g of Figure 5, the distributions of mechanical aperture (b) for both Area-1 and Area-2 shift to larger apertures and span a broader range after reaction. These findings are consistent with the distributions reported by Ellis et al.[13] for the whole fracture. When degraded zones are treated as part of the rock, the histograms shift less (panels c and g of Figure 5) relative to when the degraded zones are instead treated as a fracture (panels b and f of Figure 5).

Table 2 documents all of the major statistics of the mechanical apertures for the six meshes. After reaction, the average aperture of Area-1 doubled. For Area-2, the average aperture tripled. The maximum aperture recorded for the after reaction meshes increased much more than the average aperture, leading to larger standard deviations.

Degraded zones account for less than 15% of the fracture volumes and yet cover 70 and 80% of the fracture surfaces in Area-1 and Area-2, respectively. When the aperture distributions of the two different treatments of degraded zones are compared (Table 2), average aperture differences are 141 and 271 μm for Area-1 and Area-2, respectively. The differences are due to the relatively small fracture volume occupied by degraded zones, which is also reflected in the thickness histograms for the degraded zones that are shown in panels d and h of Figure 5. Larger standard deviations are observed when degraded zones are considered as a fracture.

Table 1 tabulates the roughness parameters. The surface Z_2 parameters are generally larger than the values reported previously,[44] which can be attributed to the fine resolution of the meshes. The D_f values calculated for all of the fracture meshes fall in the 1−2 range of a true fractal and fluctuate around 1.5, the value for a Brownian fractal profile,[50] justifying the adoption of the fractal dimension and the method used to calculate D_f in the fracture meshes.

The dissolution reactions significantly enhanced the roughness of the fracture surfaces in both Area-1 and Area-2. Both the surface Z_2 parameters and D_f increase after reactions. This trend is consistent for the upper and lower walls, as well as the

dx.doi.org/10.1021/ef302041s | Energy Fuels 2013, 27, 4221−4231

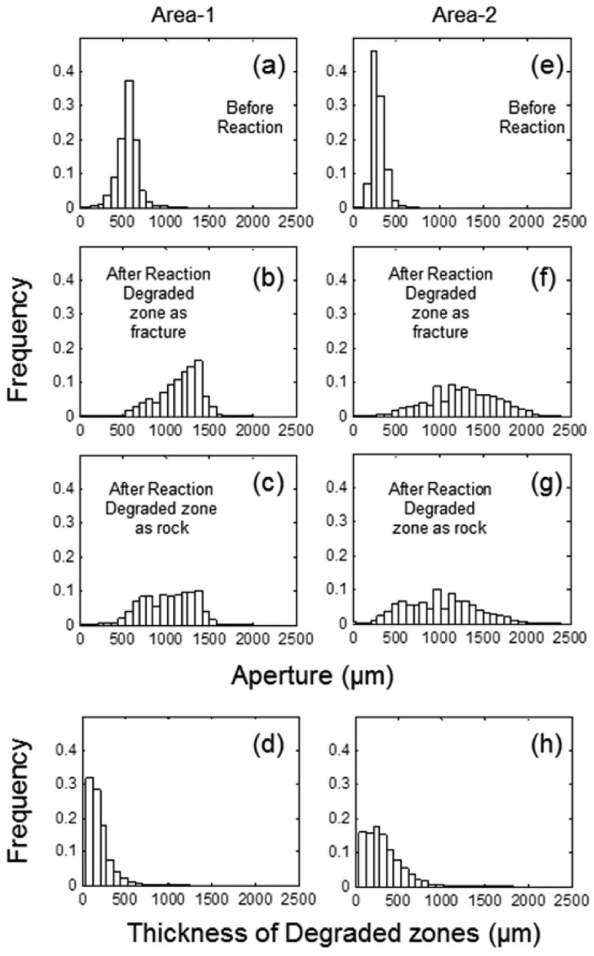

Figure 5. Histograms of the distributions of mechanical apertures for Area-1 (a) before reaction, (b) after reaction with the degraded zone treated as a fracture, and (c) after reaction with the degraded zone treated as a rock and Area-2 (e) before reaction, (f) after reaction with the degraded zone treated as a fracture, and (g) after reaction with the degraded zone treated as a rock. Histograms of the thickness of degraded zones for (d) Area-1 and (h) Area-2.

midsurface of the fracture meshes, implying that the changes of the two fracture surfaces are not perfectly correlated. However, the lower roughness of the midsurface relative to the fracture walls indicates some degree of symmetry and registry between the two fracture walls. If degraded zones are treated as a fracture, the increase in roughness relative to the before reaction meshes is limited, whereas the roughness increase is more significant when degraded zones are treated as a rock. The impacts of degraded zones on surface roughness measured by both surface Z_2 parameters and D_f are consistently observed for both areas.

Figure 6 shows the comparison between the changes in aperture (Figure 6a) and the spatial distribution of degraded zones (Figure 6b). The white regions of Figure 6b, which indicate the absence of degraded zones, are generally correlated with areas of great aperture increase shown in Figure 6a. In contrast, the presence of thick degraded zones as shown in darker color in Figure 6b coincides with some of the regions where aperture increase is limited. In regions such as the blue band at the bottom of Figure 6a, aperture increase is small and degraded zones are absent or thin, thus indicating bands of unreactive minerals. The large surface coverage of degraded zones and the variable thickness shown within degraded zones (Figure 6b) are consistent with the observation that treating the degraded zone as a rock produces the largest after reaction increase in fracture roughness.

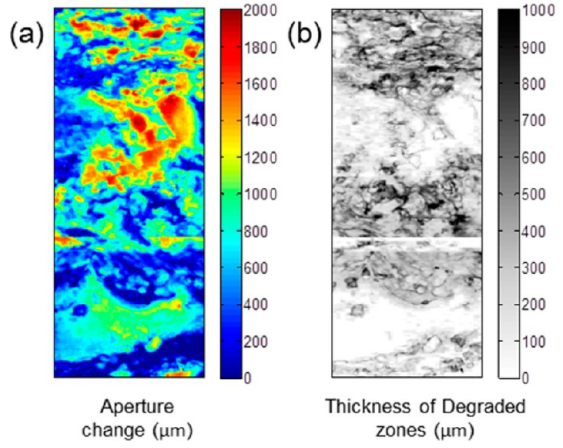

Figure 6. (a) Changes of aperture between after reaction geometry degraded zones treated as a rock and before reaction geometry of Area-2 and (b) map of the occurrence and thickness of degraded zones. The linear feature at approximately one-third of the area from the bottom is due to the fact that two scans were stitched together.

Fracture Hydrodynamic Properties. The pressure and velocity fields are shown in Figure 7. Examples of pressure fields are shown only for the before reaction meshes. The CFD-inferred T and k values of the after reaction meshes are larger than those of the before reaction meshes (Figure 8), indicating an increase in fracture hydrodynamic properties, following exposure of the fracture to CO_2-acidified brine flow. When the degraded zones within Area-1 are treated as a fracture, T increased by a factor of 8, from the value before reaction, and k increased by a factor of 4. When the degraded zones in Area-2 are treated as a

Table 2. Aperture Statistics of Six Fracture Geometries[a]

			aperture (b) (μm)					
			minimum	maximum	mean	median	standard deviation	mode
Area-1	before reaction		1269	594	594	124	594	
	after reaction	DZF	0	1998	1194	1242	242	1323
		DZR	0	1998	1053	1080	303	1296
Area-2	before reaction		810	332	324	79	270	
	after reaction	DZF	0	2484	1319	1323	390	1377
		DZR	0	2457	1048	1053	420	1026

[a]DZF, degraded zones treated as a fracture; DZR, degraded zones treated as a rock.

dx.doi.org/10.1021/ef302041s | *Energy Fuels* 2013, 27, 4221−4231

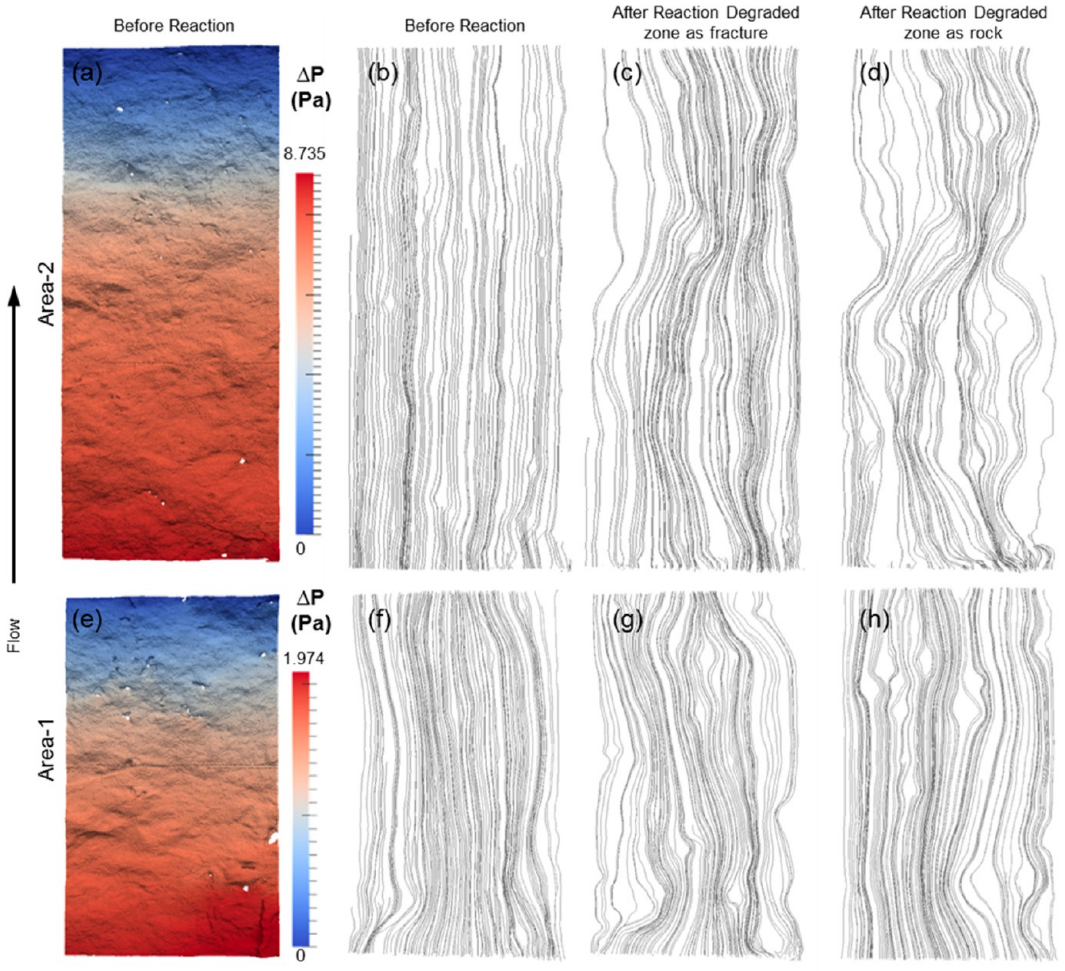

Figure 7. CFD simulation results: (a) Area-2 field of pressure difference (with respect to the outlet) in the before reaction mesh, (b–d) Area-2 velocity fields shown as streamlines for before reaction mesh, after reaction mesh with degraded zones treated as a fracture, and after reaction mesh with degraded zones treated as a rock, and (e–h) analogous for Area-1. Streamlines were generated by tracking the particles released at the inlet surface (at the bottom). In each geometry, 120 particles were released.

fracture, both T and k increased by more than 1 order of magnitude. When the degraded zones are treated as a rock, however, the margin of the increases in T and k narrowed significantly in both areas. For Area-1, T and k of the mesh for which degraded zones are treated as rocks are approximately half of the values for when degraded zones are treated as a fracture. Differences in T and k between the two after reaction meshes are even larger for Area-2.

The values of hydraulic aperture inferred from CFD simulations b_{hCFD} are consistently lower than the average b values derived directly from the xCT images (Figure 9). For Area-1, the before reaction b_{hCFD} is approximately 150 μm less than b, while the after reaction differences are twice this much. For Area-2, the initial difference between b_{hCFD} and b is approximately 100 μm, but this difference increased to more than 500 μm after reaction. The discrepancy between b and b_{hCFD} is smaller when degraded zones are treated as a fracture. The values of hydraulic aperture estimated using the 1D roughness model developed by Zimmerman and Bodvarsson[33] and the 2D LCL model[35] are also smaller than b. These values, however, are consistently larger than b_{hCFD}. In addition, the differences between hydraulic apertures estimated from the 1D and 2D models and b_{hCFD} are much larger than the uncertainty in b_{hCFD} associated with an increasing mesh density. Finally, although both b_{hCFD} and b increased following reactive flow as a result of dissolution reactions, the changes in b_{hCFD} are not proportional to the changes in b. The ratios of b_{hCFD} after reaction over b_{hCFD} before reaction are always smaller than the ratios of b, meaning that an increase in b_{hCFD} is less than an increase in b.

Impacts of Fracture Roughness. In a fracture with smooth parallel walls, b and b_h are equivalent, and therefore, b can be used directly to estimate fracture hydrodynamic properties. Monitoring effluent chemistry and using mass balance provide one way to quantify dissolution and infer changes in average b.[30] Alterations in b because of reactions can also be calculated from reactive transport modeling.[19,37,51] In addition, applications of imaging techniques, such as xCT scans[25,27] and light transmission,[24] allow for the characterization of fracture morphology and b from images.

For rough-wall fractures, b_h deviates from b (e.g., Figure 9), and the extent of the deviation is primarily controlled by the degree of roughness. It has been pointed out in previous work[16,18,22,30] and confirmed in our study that reactions change both the volume and roughness of the fracture. Moving from the before reaction geometry to the after reaction geometry where the degraded zones are treated as a rock, fracture roughness increases and streamlines in the fractures become more tortuous, deviating more from the parallel streamlines that define b and b_h

dx.doi.org/10.1021/ef302041s | Energy Fuels 2013, 27, 4221–4231

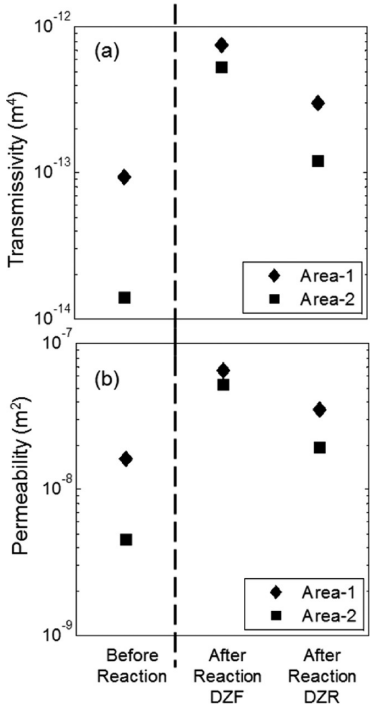

Figure 8. CFD simulation results of (a) transmissivity and (b) permeability of all six fracture geometries. DZF, degraded zones treated as a fracture; DZR, degraded zones treated as a rock.

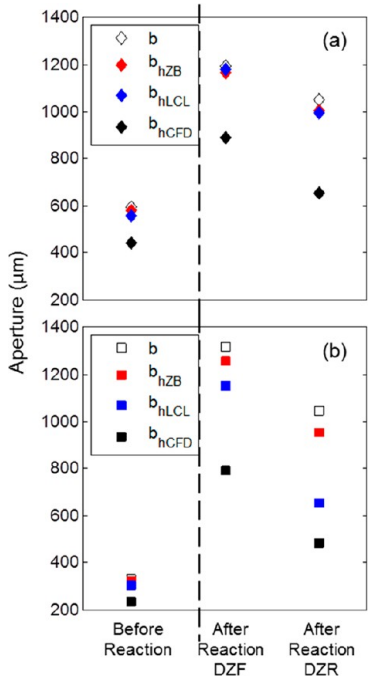

Figure 9. Mechanical aperture (b) and hydraulic apertures inferred from the 1D roughness model developed by Zimmerman and Bodvarsson (b_{hZB}), 2D LCL model (b_{hLCL}), and CFD simulations (b_{hCFD}) for (a) Area-1 and (b) Area-2. DZF, degraded zones treated as a fracture; DZR, degraded zones treated as a rock.

equivalence (Figure 7). As a result, the deviation of b_h from b, as measured by the ratio between b_h and b, grows as roughness increases (Figure 10). This variation in the deviation of b_h from b greatly complicates quantification of the changes in hydrodynamics properties caused by reaction. For example, for the

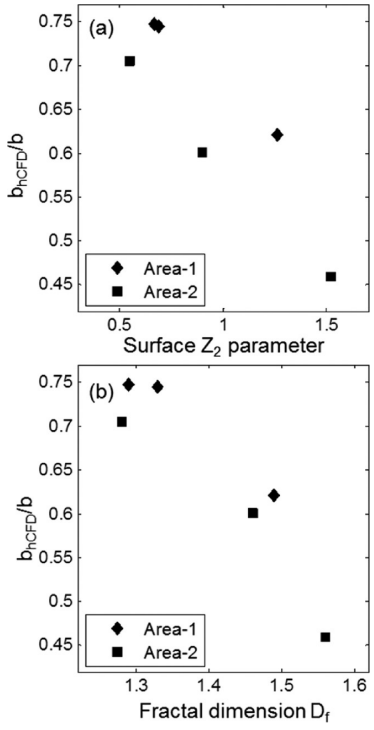

Figure 10. Ratio of the hydraulic aperture inferred from CFD simulations over mechanical aperture (b_{hCFD}/b) in comparison to (a) surface Z_2 parameter and (b) fractal dimension D_f of the midsurface.

after reaction geometry of Area-2 with the degraded zone treated as a rock, b has tripled, while b_h shows only doubling (Figure 9b). Therefore, if a 3-fold increase in b_h is assumed simply on the basis of the observed changes in b, k and T are overestimated by more than 100 and 200%, respectively, because of the power law relationships (eqs 2 and 3). Because k and T are the major inputs for most hydrodynamic models, these overestimations will propagate into the model predictions of key performance parameters, such as leakage risks of CO_2 storage and shale gas production.

To account for variations in b along a fracture, Tsang and Witherspoon[31] used a weighted average of b to estimate T. A subsequent study observed that the ratio of b_h and b is related only to the variance of the log aperture, and hence, b_h can be estimated from the distribution of fracture b.[32] On the basis of a comprehensive review, Zimmerman and Bodvarsson[33] proposed a model to account for the impacts of roughness by incorporating the standard deviation of b and contact area ratio. In addition to the statistical approach, the 2D LCL model is also widely used. In fractures with low roughness, its capability of capturing fracture hydrodynamic properties was justified and the uncertainties caused by the model were considered negligible compared to other processes.[37]

However, for the fracture geometries in this study, both the 1D statistical model developed by Zimmerman and Bodvarsson[33] and 2D LCL model that assumes cubic law applied locally largely overestimate the flow and failed to fully capture the impact of the roughness. The poor performance of these modeling approaches is primarily rooted in the severe roughness caused by preferential dissolutions of calcite relative to less soluble silicate and dolomite.

Mineral Heterogeneity and Evolution of Fracture Hydrodynamic Properties. Changes of fracture roughness after exposure to acidic flow are primarily controlled by the

dx.doi.org/10.1021/ef302041s | Energy Fuels 2013, 27, 4221−4231

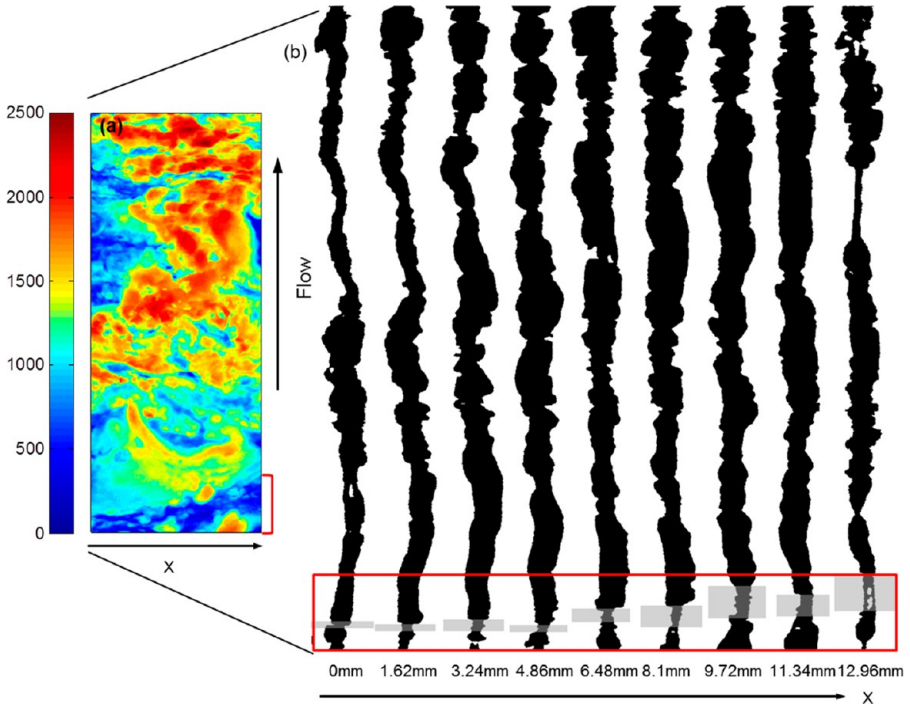

Figure 11. (a) Aperture map (μm) of after reaction geometry of Area-2 with degraded zones treated as a fracture and (b) sections of the fracture along the flow direction sampled every 1.62 mm. Gray boxes highlight the areas where aperture increase is minimal, corresponding to the blue band near the bottom of the Area-2 fracture.

spatial distribution of reactive minerals and less soluble minerals. One type of sedimentary feature that results in a roughness increase is banding of reactive and unreactive minerals. The cross-sections of the fracture along the flow direction at nine x values shown in Figure 11 illustrate that, although extensive dissolution has resulted in substantial b enlargement, there are still some regions along the flow pathway where aperture increase is limited because of a contiguous transverse stricture, which exists because of a sedimentary layer of relatively insoluble minerals.

Mineral heterogeneity also affects flow by creation of reaction degraded zones. Two core-flooding studies on different carbonate rocks observed the formation of "degraded zones" along the fracture boundary, following the flow of acidified brines.[13,30] The formation of degraded zones results from the dissolution of calcite from within a matrix of relatively insoluble minerals (e.g., dolomite and silicates). Our study demonstrated that the range of possible transmissivity outcomes is large dependent upon whether or not there is flow through the degraded zones, even though they account for only a relatively small fraction of the fracture volume. The primary reasons are highlighted by the degraded zone occurrence and thickness map shown for Area-2 in Figure 6b, where degraded zones cover a large fraction of the fracture surface and have a large impact on roughness (Table 1). The large impact of degraded zones on fracture roughness is also consistent with previous findings,[52] which documented higher roughness for the coated natural fracture surface than uncoated surfaces.

Our studies on the impacts of geometric alterations on fracture hydrodynamic properties can lend some insight for predicting their evolution as a result of longer exposure to CO_2-acidified brine. For the case of banding of calcite with dolomite, roughness increased dramatically because of preferential dissolution of calcite. However, because the preferential dissolution of calcite is due to differential solubilities of the two minerals, longer term contact with CO_2-acidified brine will cause dolomite to also dissolve. Consequently, constraints on flow by the dolomite bands will be reduced and fracture T and k will increase. Because dolomite dissolves slowly compared to calcite, roughness will keep growing, but the effect of this roughness may diminish as b increases. Therefore, an increase of fracture hydrodynamic properties will be disproportional to the fracture volume increase. If, instead, calcite is banded with non-reactive minerals, such as clay minerals, the non-reactive bands will persist as constraints on the flow and fracture hydrodynamic properties may change only negligibly in response to preferential dissolution of calcite. However, sharp changes in fracture hydrodynamic properties may happen if the geomechanical strength of the non-reactive bands is compromised.

In rocks in which minerals are mixed more homogeneously, i.e., not in bands parallel to sedimentary bedding, preferential dissolution of calcite leads to the formation of the degraded zone. If the fluid in the degraded zone is hydraulically isolated, existence of the degraded zone will serve as a protective layer against further erosion, because ions need to diffuse through the degraded zone to reach the reaction front. If the degraded zones are composed of dolomite, dolomite will start to dissolve, given a longer exposure to CO_2-acidified brine, and the degraded zones will evolve toward the direction of the extreme scenario when degraded zones are considered as a fracture. Dissolution of dolomite may be faster compared to the fracture surface because of the increase of the reactive surface area created by the degraded zones. In contrast, if the degraded zones are composed of aluminosilicates left after preferential dissolution of calcite, they will be preserved, even with a longer exposure to reactive fluid, and the constraints on flow will remain. Another possibility in this case is decohesion of the aluminosilicates. As inferred from the experimental observations by Ellis et al.[14] and Noiriel et al.,[30]

dx.doi.org/10.1021/ef302041s | *Energy Fuels* 2013, 27, 4221−4231

the mobilized particles will be transported by the flow and may be carried through the fracture, which leads to b increasing and smoothing of fracture walls, or they may be trapped and clog the flow pathway, which results in a reduction in fracture hydrodynamic properties.

CONCLUSION

The discrepancy between hydraulic aperture, b_h, and mechanical aperture, b, and the incapability of the 1D statistical model and 2D LCL model to capture the differences imply that prudence is required when studying the impacts of reactive transport on fracture hydrodynamic properties. Coupling the detailed fracture geometry reconstructed from xCT images and CFD simulations provides more accurate estimations of fracture hydrodynamic properties. Our study has not only successfully applied this method but also extended it to study true geometrical alterations, high roughness and degraded zones, caused by reactive flow. We used xCT images collected before and after a flow-through experiment and CFD simulations to study the changes of fracture hydrodynamic properties as a result of reactive flow. We found that modifications of hydrodynamic properties are constrained by both the volume dissolved and the development of specific geometric features that can be traced to the underlying mineralogy. In our study, the increase in fracture hydrodynamic properties is mitigated by an increase in roughness caused by zones of banded reactive and non-reactive minerals and the creation of degraded zones. The high degrees of roughness caused by complex mineralogical spatial distributions lead to large discrepancy between b and b_h calculated from CFD simulations. In such cases, the use of b that can be derived from imaging techniques, reactive transport modeling, and experimental effluent analyses to estimate fracture hydrodynamic properties and their evolution will result in overestimation of permeability and transmissivity by a factor of 2 or more. In addition, the 1D statistical model and the 2D LCL model failed to capture flow accurately and overestimate the hydrodynamic properties relative to the CFD simulations. Therefore, if b_h estimated from the 1D and 2D models are used to estimate hydrodynamic properties, the errors will propagate into subsequent modeling, leading to overestimation of leakage risks or production prediction. More experimental studies correlating mineralogical spatial distribution and geometric alterations are needed in the future, as well as the efforts dedicated to incorporating the impacts of the resultant roughness efficiently. Such studies will benefit parametrization of the large-scale models used to predict leakage of CO_2 from geologic storage reservoirs and gas from hydraulically fractured shale formations.

AUTHOR INFORMATION

Corresponding Author

*E-mail: cap@princeton.edu.

Present Address

‡Brian R. Ellis: Department of Civil and Environmental Engineering, University of Michigan, Ann Arbor, Michigan 48109, United States.

Notes

Disclaimer: Neither the U.S. government nor any agency thereof, nor any of their employees, makes any warranty, express or implied, or assumes any legal liability or responsibility for the accuracy, completeness, or usefulness of any information, apparatus, product, or process disclosed or represents that its use would not infringe privately owned rights. Reference herein to any specific commercial product, process, or service by trade name, trademark, manufacturer, or otherwise does not necessarily constitute or imply its endorsement, recommendation, or favoring by the U.S. government or any agency thereof. The views and opinions of authors expressed herein do not necessarily state or reflect those of the U.S. government or any agency thereof.

The authors declare no competing financial interest.

ACKNOWLEDGMENTS

This work is funded by Department of Energy (DOE) awards DE-FE0000749 and DE-FG02-09ER64748, as well as by National Science Foundation (NSF) Grant CBET-1134397. Additional support came from the National Energy Technology Laboratory's ongoing research under the RES contract DE-FE0004000. We also thank the anonymous reviewers for their insightful comments, which led to valuable improvements in the manuscript.

REFERENCES

(1) Bonnet, E.; Bour, O.; Odling, N. E.; Davy, P.; Main, I.; Cowie, P.; Berkowitz, B. Scaling of fracture systems in geological media. *Rev. Geophys.* **2001**, *39*, 347−383.

(2) Singurindy, O.; Berkowitz, B. The role of fractures on coupled dissolution and precipitation patterns in carbonate rocks. *Adv. Water Resour.* **2005**, *28*, 507−521.

(3) Curtis, J. B. Fractured shale−gas systems. *AAPG Bull.* **2002**, *86*, 1921−1938.

(4) Long, J. C. S.; Ewing, R. C. Yucca Mountain: Earth-science issues at a geologic repository for high-level nuclear waste. *Annu. Rev. Earth Planet. Sci.* **2004**, *32*, 363−401.

(5) Wood, C. P.; Brathwaite, R. L.; Rosenberg, M. D. Basement structure, lithology and permeability at Kawerau and Ohaaki geothermal fields, New Zealand. *Geothermics* **2001**, *30*, 461−481.

(6) Iding, M.; Ringrose, P. Evaluating the impact of fractures on the performance of the In Salah CO_2 storage site. *Int. J. Greenhouse Gas Control* **2010**, *4*, 242−248.

(7) Griffith, C. A.; Dzombak, D. A.; Lowry, G. V. Physical and chemical characteristics of potential seal strata in regions considered for demonstrating geological saline CO_2 sequestration. *Environ. Earth Sci.* **2011**, *64*, 925−948.

(8) Park, C.; Taron, J.; Gorke, U.; Singh, A. K.; Kolditz, O. The fluidal interface is where the action is in CO_2 sequestration and storage: Hydromechanical analysis of mechanical failure. *Proceedings of the 10th International Conference on Greenhouse Gas Control Technologies, Sept 19−23, 2010*; Elsevier, Ltd.: Amsterdam, The Netherlands, 2011; Vol. 4, pp 3691−3698.

(9) Gor, G. Y.; Elliot, T. R.; Prevost, J. H. Effects of thermal stresses on caprock integrity during CO_2 storage. *Int. J. Greenhouse Gas Control* **2013**, *12*, 300−309.

(10) Noiriel, C.; Renard, F.; Doan, M.; Gratier, J. Intense fracturing and fracture sealing induced by mineral growth in porous rocks. *Chem. Geol.* **2010**, *269*, 197−209.

(11) Gherardi, F.; Xu, T.; Pruess, K. Numerical modeling of self-limiting and self-enhancing caprock alteration induced by CO_2 storage in a depleted gas reservoir. *Chem. Geol.* **2007**, *244*, 103−129.

(12) Andreani, M.; Gouze, P.; Luquot, L.; Jouanna, P. Changes in seal capacity of fractured claystone caprocks induced by dissolved and gaseous CO_2 seepage. *Geophys. Res. Lett.* **2008**, DOI: 10.1029/2008GL034467.

(13) Ellis, B.; Peters, C.; Fitts, J.; Bromhal, G.; McIntyre, D.; Warzinski, R.; Rosenbaum, E. Deterioration of a fractured carbonate caprock exposed to CO_2-acidified brine flow. *Greenhouse Gases: Sci. Technol.* **2011**, *1*, 248−260.

(14) Ellis, B. R.; Fitts, J. P.; Bromhal, G. S.; McIntyre, D. L.; Tappero, R.; Peters, C. A. Dissolution-driven permeability reduction of a fractured

carbonate caprock. *Environ. Eng. Sci.* **2013**, DOI: 10.1089/ees.2012.0337.
(15) Grieser, B.; Wheaton, B.; Magness, B.; Blauch, M.; Loghry, R. Surface reactive fluid's effect on shale. *Proceedings of the SPE Production and Operations Symposium, April 1−3, 2007*; Society of Petroleum Engineers (SPE): Oklahoma City, OK, 2007; pp 438−444.
(16) Detwiler, R.; Glass, R.; Bourcier, W. Experimental observations of fracture dissolution: The role of Peclet number on evolving aperture variability. *Geophys. Res. Lett.* **2003**, *30*, 1648−1651.
(17) Detwiler, R. Experimental observations of deformation caused by mineral dissolution in variable-aperture fractures. *J. Geophys. Res.* **2008**, DOI: 10.1029/2008JB005697.
(18) O'Brien, G. S.; Bean, C. J.; McDermott, F. Numerical investigations of passive and reactive flow through generic single fractures with heterogeneous permeability. *Earth Planet. Sci. Lett.* **2003**, *213*, 271−284.
(19) Chaudhuri, A.; Rajaram, H.; Viswanathan, H. Alteration of fractures by precipitation and dissolution in gradient reaction environments: Computational results and stochastic analysis. *Water Resour. Res.* **2008**, DOI: 10.1029/2008WR006982.
(20) Detwiler, R.; Rajaram, H. Predicting dissolution patterns in variable aperture fractures: Evaluation of an enhanced depth-averaged computational model. *Water Resour. Res.* **2007**, DOI: 10.1029/2006WR005147.
(21) Tartakovsky, D. M.; Dentz, M.; Lichtner, P. C. Probability density functions for advective-reactive transport with uncertain reaction rates. *Water Resour. Res.* **2009**, DOI: 10.1029/2008WR007383.
(22) Verberg, R.; Ladd, A. J. C. Simulation of chemical erosion in rough fractures. *Phys. Rev. E: Stat., Nonlinear, Soft Matter Phys.* **2002**, *65* (5, Part 2), 056311.
(23) Szymczak, P.; Ladd, A. Wormhole formation in dissolving fractures. *J. Geophys. Res.* **2009**, DOI: 10.1029/2008JB006122.
(24) Detwiler, R.; Pringle, S.; Glass, R. Measurement of fracture aperture fields using transmitted light: An evaluation of measurement errors and their influence on simulations of flow and transport through a single fracture. *Water Resour. Res.* **1999**, *35*, 2605−2617.
(25) Gouze, P.; Noiriel, C.; Bruderer, C.; Loggia, D.; Leprovost, R. X-ray tomography characterization of fracture surfaces during dissolution. *Geophys. Res. Lett.* **2003**, DOI: 10.1029/2002GL016755.
(26) Werth, C. J.; Zhang, C.; Brusseau, M. L.; Oostrom, M.; Baumann, T. A review of non-invasive imaging methods and applications in contaminant hydrogeology research. *J. Contam. Hydrol.* **2010**, *113*, 1−24.
(27) Karpyn, Z. T.; Grader, A. S.; Halleck, P. M. Visualization of fluid occupancy in a rough fracture using micro-tomography. *J. Colloid Interface Sci.* **2007**, *307*, 181−187.
(28) Wildenschild, D.; Sheppard, A. P. X-ray imaging and analysis techniques for quantifying pore-scale structure and processes in subsurface porous medium systems. *Adv. Water Resour.* **2013**, *51*, 217−246.
(29) Nicholl, M.; Rajaram, H.; Glass, R.; Detwiler, R. Saturated flow in a single fracture: Evaluation of the Reynolds equation in measured aperture fields. *Water Resour. Res.* **1999**, *35*, 3361−3373.
(30) Noiriel, C.; Made, B.; Gouze, P. Impact of coating development on the hydraulic and transport properties in argillaceous limestone fracture. *Water Resour. Res.* **2007**, DOI: 10.1029/2006WR005379.
(31) Tsang, Y.; Witherspoon, P. Hydromechanical behavior of a deformable rock fracture subject to normal stress. *J. Geophys. Res.* **1981**, *86*, 9287−9298.
(32) Renshaw, C. On the relationship between mechanical and hydraulic apertures in rough-walled fractures. *J. Geophys. Res.* **1995**, *100*, 24629−24636.
(33) Zimmerman, R.; Bodvarsson, G. Hydraulic conductivity of rock fractures. *Transp. Porous Media* **1996**, *23*, 1−30.
(34) Cvetkovic, V.; Selroos, J. O.; Cheng, H. Transport of reactive tracers in rock fractures. *J. Fluid Mech.* **1999**, *378*, 335−356.
(35) James, S. C.; Chrysikopoulos, C. V. Transport of polydisperse colloids in a saturated fracture with spatially variable aperture. *Water Resour. Res.* **2000**, *36*, 1457−1465.
(36) Ghassemi, A.; Kumar, G. S. Changes in fracture aperture and fluid pressure due to thermal stress and silica dissolution/precipitation induced by heat extraction from subsurface rocks. *Geothermics* **2007**, *36*, 115−140.
(37) Yasuhara, H.; Elsworth, D. A numerical model simulating reactive transport and evolution of fracture permeability. *Int. J. Numer. Anal. Methods Geomech.* **2006**, *30*, 1039−1062.
(38) Petchsingto, T.; Karpyn, Z. T. Deterministic modeling of fluid flow through a CT-scanned fracture using computational fluid dynamics. *Energy Sources, Part A* **2009**, *31*, 897−905.
(39) Crandall, D.; Bromhal, G.; Karpyn, Z. T. Numerical simulations examining the relationship between wall-roughness and fluid flow in rock fractures. *Int. J. Rock Mech. Min. Sci.* **2010**, *47*, 784−796.
(40) Javadi, M.; Sharifzadeh, M.; Shahriar, K. A new geometrical model for non-linear fluid flow through rough fractures. *J. Hydrol.* **2010**, *389*, 18−30.
(41) Snow, D. Anisotropic permeability of fractured media. *Water Resour. Res.* **1969**, *5*, 1273−1289.
(42) Otsu, N. A threshold selection method from gray-level histograms. *IEEE Trans. Syst., Man Cybern.* **1979**, *9*, 62−66.
(43) Fang, Q.; Boas, D. A. Tetrahedral mesh generation from volumetric binary and grayscale images. *Proceedings of the 2009 IEEE International Symposium on Biomedical Imaging: From Nano to Macro, ISBI 2009, June 28−July 1, 2009*; IEEE Computer Society: Boston, MA, 2009; pp 1142−1145.
(44) Belem, T.; Homand-Etienne, F.; Souley, M. Quantitative parameters for rock joint surface roughness. *Rock Mech. Rock Eng.* **2000**, *33*, 217−242.
(45) Dougan, L. T.; Addison, P. S.; McKenzie, W. M. C. Fractal analysis of fracture: A comparison of dimension estimates. *Mech. Res. Commun.* **2000**, *27*, 383−392.
(46) Yastrebov, V. A.; Anciaux, G.; Molinari, J. Contact between representative rough surfaces. *Phys. Rev. E: Stat., Nonlinear, Soft Matter Phys.* **2012**, *86*, 035601.
(47) Tsang, Y. W.; Witherspoon, P. A. Dependence of fracture mechanical and fluid flow properties on fracture roughness and sample size. *J. Geophys. Res.* **1983**, *88*, 2359−2366.
(48) Brush, D. J.; Thomson, N. R. Fluid flow in synthetic rough-walled fractures: Navier−Stokes, Stokes, and local cubic law simulations. *Water Resour. Res.* **2003**, DOI: 10.1029/2002WR001346.
(49) Konzuk, J. S.; Kueper, B. H. Evaluation of cubic law based models describing single-phase flow through a rough-walled fracture. *Water Resour. Res.* **2004**, DOI: 10.1029/2003WR002356.
(50) Edenhofer, O.; Knopf, B.; Barker, T.; Baumstark, L.; Bellevrat, E.; Chateauaaa, B.; Criqui, P.; Isaac, M.; Kitous, A.; Kypreos, S.; Leimbach, M.; Lessmann, K.; Magne, B.; Scrieciu, S.; Turton, H.; van Vuuren, D. P. The economics of low stabilization: model comparison of mitigation strategies and costs. *Energy J.* **2010**, *31*, 11−48.
(51) Rawal, C.; Ghassemi, A. Fracture aperture change in response to reactive transport of silica and thermoelastic effects. *Proceedings of the Canada Rock Mechanics Symposium 2008, June 29−July 2, 2008*; Omnipress: San Francisco, CA, 2008; Paper 08-253.
(52) Weisbrod, N.; Nativ, R.; Adar, E.; Ronen, D.; Ben-Nun, A. Impact of coating and weathering on the properties of chalk fracture surfaces. *J. Geophys. Res.: Solid Earth* **2000**, *105*, 27853−27864.